Commun Nonlinear Sci Numer Simulat 30 (2016) 84–100

Contents lists available at ScienceDirect

Commun Nonlinear Sci Numer Simulat

journal homepage: www.elsevier.com/locate/cnsns

A phase-field fluid modeling and computation with interfacial profile correction term

Yibao Li [a], Jung-Il Choi [b], Junseok Kim [c,*]

[a] School of Mathematics and Statistics, Xi'an Jiaotong University, Xi'an 710049, China
[b] Department of Computational Science and Engineering, Yonsei University, Seoul 120-749, Republic of Korea
[c] Department of Mathematics, Korea University, Seoul 136-713, Republic of Korea

ARTICLE INFO

Article history:
Received 6 February 2015
Revised 13 June 2015
Accepted 15 June 2015
Available online 22 June 2015

Keywords:
Cahn–Hilliard equation
Mass conservation
Navier–Stokes equation
Two-phase fluid flow
Multigrid method

ABSTRACT

We present a new phase-field fluid model and computation with minimized Cahn–Hilliard (CH) dynamics. Using the CH equation, the internal structure of the interface layer is determined by explicit smoothing flow discontinuities. This method greatly simplifies gridding, discretization, and handling of topological changes. The original CH equation, however, has intrinsic dynamics such as interface length minimization, i.e., the motion by minus the Laplacian of the mean curvature. When the CH equation is applied to the modeling of multiphase fluid flows, we want to minimize its interface length minimization property. The surface tension formulation also requires the multiphase fluid interface to be a hyperbolic tangent profile. Typically, under the advection of flow, the interfacial transition is not a hyperbolic tangent profile, i.e., it is too compressed or sharpened. Even though the original CH dynamics conserves the total mass, the enclosed area obtained by its interface is not preserved. To overcome these shortcomings, we propose a modified CH equation with an interfacial profile correction term. Several numerical examples are presented to show the accuracy of the proposed method. The numerical results demonstrate that the proposed modified CH equation preserves the enclosed area better than the original CH equation.

1. Introduction

We present a phase-field fluid model and computation with minimized Cahn–Hilliard (CH) dynamics. The original CH equation was introduced to model spinodal decomposition in binary alloys [1] and arises from the Helmholtz free energy functional

$$\mathcal{E}_{\mathrm{CH}}(\phi) = \int_{\Omega} \left(F(\phi) + \frac{\epsilon^2}{2} |\nabla \phi|^2 \right) d\mathbf{x},$$

where $\Omega \subset \mathbb{R}^d$ (d is the space dimension), $F(\phi) = 0.25(\phi^2 - 1)^2$, and ϵ is a positive constant. The quantity $\phi(\mathbf{x}, t)$ is defined as the difference between the mole fractions of binary mixtures. The CH equation takes the form

$$\frac{\partial \phi}{\partial t}(\mathbf{x}, t) = M \Delta \mu(\mathbf{x}, t), \mathbf{x} \in \Omega, 0 < t \leq T, \tag{1}$$

* Corresponding author. Tel.: +82 2 3290 3077; fax: +82 2 929 8562.
E-mail addresses: yibaoli@mail.xjtu.edu.cn (Y. Li), jic@yonsei.ac.kr (J.-I. Choi), cfdkim@korea.ac.kr (J. Kim).
URL: http://gr.xjtu.edu.cn/web/yibaoli (Y. Li), http://math.korea.ac.kr/~cfdkim (J. Kim)

http://dx.doi.org/10.1016/j.cnsns.2015.06.012
1007-5704/

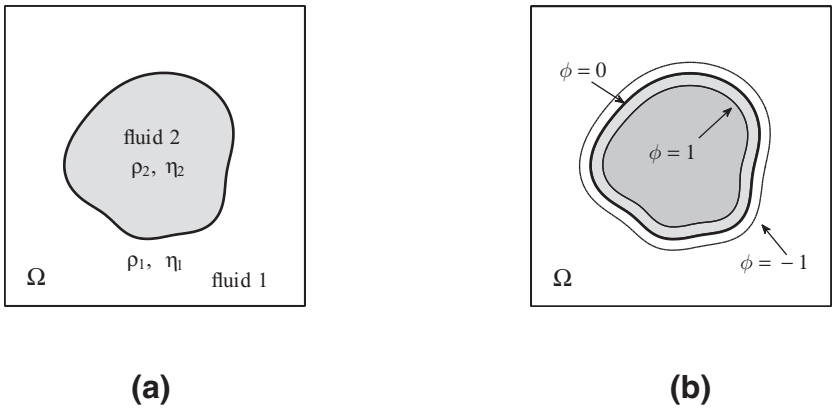

Fig. 1. Schematic illustration of the computational problem. (a) Two fluids. (b) Phase-field.

$$\mu(\mathbf{x},t) = F'(\phi(\mathbf{x},t)) - \epsilon^2\Delta\phi(\mathbf{x},t), \tag{2}$$

$$\mathbf{n}\cdot\nabla\mu(\mathbf{x},t) = 0, \mathbf{x}\in\partial\Omega, \tag{3}$$

where M is the positive constant mobility and $\mathbf{n}$ is the outward normal vector at the boundary. The CH equation can be derived from a constrained gradient flow in the $\dot{H}^{-1}$ Hilbert space. It guarantees that the total free energy $\mathcal{E}_{\mathrm{CH}}(\phi)$ decreases in time t [2]. The solution $\phi(\mathbf{x}, t)$ to Eqs. (1)–(3) possesses the properties that the total mass is conserved, i.e., $d(\int_\Omega \phi d\mathbf{x})/dt = 0$, and the total energy $\mathcal{E}_{\mathrm{CH}}(t)$ decreases with time. Governing equations for the flow are obtained by coupling the momentum and CH equations. The CH equation has been successfully applied to a wide range of problems in materials science [5,6], biology [7,8], image processing [9,10], surface/volume reconstruction [11], and fluid dynamics [12–23,25–44] (see the recent review paper [32] and the references therein). Using the CH equation, the internal structure of the interface layer can be determined by explicit smoothing flow discontinuities. This method greatly simplifies gridding, discretization, and handling of topological changes. The momentum equation is a modified Navier–Stokes equation:

$$\rho(\phi)(\mathbf{u}_t + \mathbf{u}\cdot\nabla\mathbf{u}) = -\nabla p + \nabla\cdot(\eta(\phi)(\nabla\mathbf{u} + \nabla\mathbf{u}^T)) + \sigma\mathbf{SF}(\phi) + \rho(\phi)\mathbf{g}, \tag{4}$$

$$\nabla\cdot\mathbf{u} = 0, \tag{5}$$

where $\mathbf{u}$ is the velocity, p is the pressure, σ is the surface tension coefficient, and $\mathbf{g} = (0, -g)$ is the gravity. The density $\rho(\phi)$ and viscosity $\eta(\phi)$ are assumed to be linearly related to the concentration ϕ:

$$\rho(\phi) = \rho_1(1-\phi)/2 + \rho_2(1+\phi)/2 \quad \text{and} \quad \eta(\phi) = \eta_1(1-\phi)/2 + \eta_2(1+\phi)/2,$$

where ρ_1 and ρ_2 are the densities of fluid 1 and fluid 2, respectively. η_1 and η_2 are the viscosities of fluid 1 and fluid 2, respectively. A schematic illustration of the computational problem is shown in Fig. 1.

The interfacial force $\mathbf{SF}(\phi)$ satisfying the Laplace–Young condition is defined as $\mathbf{SF}(\phi) = -\kappa(\phi)\delta(\phi)\mathbf{n}_s(\phi)$, where $\mathbf{n}_s(\phi)$ is the outward unit normal vector to the interface of the two phases, $\kappa(\phi)$ is the mean curvature, and $\delta(\phi)$ is the surface Dirac-delta distribution. Furthermore, $\mathbf{n}_s$, κ and δ are given by $\mathbf{n}_s = -\nabla\phi/|\nabla\phi|$, $\kappa = \nabla\cdot\mathbf{n}_s$, and $\delta = \epsilon\alpha|\nabla\phi|^2$ [3], respectively. The CH dynamics is characterized by transition layers between two phases with an equilibrium profile [4]:

$$\phi^{eq}(r) = \tanh(r/(\sqrt{2}\epsilon)). \tag{6}$$

The local coordinate r is from the outside of the surface to the inside normally and is zero at the interface. With the equilibrium composition profile, α can be computed as $\alpha = 3\sqrt{2}/4$ by solving $\epsilon\alpha\int_{-\infty}^{\infty}(\phi_r^{eq})^2 dr = 1$. Thus, the interface of the two phases should be a hyperbolic tangent profile to accurately calculate the surface tension force. However, when an advection term is added, the interface of the two phases may not be a hyperbolic tangent profile. The original CH equation has intrinsic dynamics such as interface length minimization, i.e., the motion by minus the Laplacian of the mean curvature [45]. Thus, when the CH equation is applied to model multiphase fluid flows, we want to minimize its interface length minimization property. In practice, when a large time step or coarse grid is used, the interface length minimization property of the CH equation is significant. Furthermore, although the CH dynamics conserves the total mass over the entire domain, it typically does not preserve the area enclosed by the interface of the two phases. Yue et al. [46] noted that the equilibrium solution of the CH equation is similar to, but not equal to a hyperbolic tangent profile; the solution to the CH equation is in $[-1+\beta, 1+\beta]$, where β is a small value related to the thickness ϵ, the volume of the whole computational domain and drop. This is because the total energy can be reduced by shrinking the drop while simultaneously shifting the bulk ϕ slightly away from the initial values (see Fig. 2). Therefore, the CH

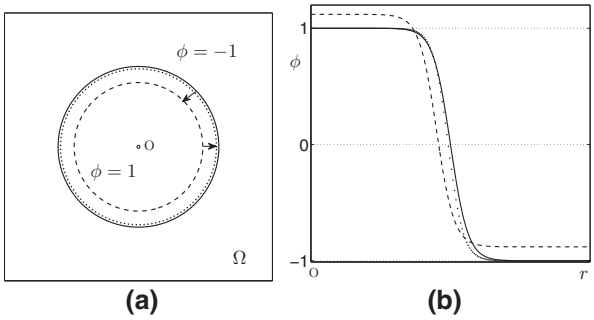

Fig. 2. Schematic illustration of the shifting of a circular drop. (a) The plots of ϕ in two-dimensional view. The solid, dashed, and dotted lines denote the zero level set of the initial ϕ, steady state of ϕ obtained by the original CH equation, and the hyperbolic tangent profile (Eq. (6)), respectively. (b) The plots of ϕ in cross view. Note that a similar schematic illustration can be found in [46].

dynamics typically does not preserve the enclosed mass computed by the zero level of the two phases. Theoretically, as $\epsilon \to 0$, the CH dynamics conserves the mass. In actual implementation, however, the interface has a small but finite thickness.

Since the CH equation satisfies the total conservation of mass, if the values in the bulk of each component are almost ± 1 and if the interface of the two phases is a hyperbolic tangent profile, then the mass is conserved in each component. The mass loss in the original CH equation works by shifting the interface of the two phases and then shrinking the bulk ϕ. This forces the hyperbolic tangent profile to reduce the mass loss (see Fig. 2) and improve the accuracy of the surface tension force.

The objective of this paper is to propose a new conservative numerical method for the CH equation with an interfacial profile correction term. The CH equation is discretized using a finite difference scheme. The resulting scheme is solved by a fast multigrid method. Several numerical examples are presented to demonstrate the accuracy of the proposed method.

Note that in a different context, Folch et al. [22,23] presented a phase-field model for the dynamics of the interface between two immiscible fluids with arbitrary viscosity contrast in a rectangular Hele–Shaw cell. The Allen–Cahn (AC) equation [24] was used as the phase-field model together with an additional term, $-\epsilon^2\nabla\cdot(\nabla\phi/|\nabla\phi|)|\nabla\phi|$ in order to cancel out the local AC dynamics of the interface, i.e., the motion by mean curvature. The modified phase-field model yields the Hele–Shaw equation in the sharp-interface limit. Another modified phase-field approach is proposed to study the interaction between a vesicle and an external hydrodynamic flow lies in the free-boundary character of it vesicle shape [15], where a correction term is added to make cells tumble precisely in order to reduce the dissipation when the cell concentration is low.

This paper is organized as follows. In Section 2, we describe the phase-field fluid model and computation with minimized CH dynamics. In Section 3, we describe the numerical solution. We perform numerical experiments and present the results in Section 4. Conclusions are presented in Section 5.

2. The proposed model

To force the interface of the two phases to be a hyperbolic tangent profile, we propose a new modified CH equation:

$$\frac{\partial\phi}{\partial t} = M\Delta\mu + \lambda M\left(\Delta\phi - \frac{1}{\sqrt{2}\epsilon}\nabla\cdot\left((1-\phi^2)\frac{\nabla\phi}{|\nabla\phi|}\right)\right), \tag{7}$$

$$\mu = F'(\phi) - \epsilon^2\Delta\phi, \tag{8}$$

$$\frac{\partial\mu}{\partial\mathbf{n}} = 0, \mathbf{x}\in\partial\Omega, \tag{9}$$

where the positive constant λ is related to the gradient energy coefficient ϵ, which is a measure of the transition region between two phases. Also, λ is related to the flow velocity when the advection term is added. The last term in Eq. (7) is the fidelity term that forces the interface of the two phases to be a hyperbolic tangent profile. The new modified CH equation is derived from the following total energy:

$$\begin{aligned}\mathcal{E}(\phi) &= \mathcal{E}_{\mathrm{CH}}(\phi) + \mathcal{E}_F(\phi)\\ &= \int_\Omega\left(F(\phi) + \frac{\epsilon^2}{2}|\nabla\phi|^2\right)d\mathbf{x} + \int_\Omega\frac{\lambda}{2}\left(\frac{1-\phi^2}{\sqrt{2}\epsilon} - |\nabla\phi|\right)^2 d\mathbf{x},\end{aligned} \tag{10}$$

where $\mathcal{E}_F(\phi)$ is an energy functional that forces the phase-field profile to be a hyperbolic tangent profile of the following form [47]:

$$\phi(\mathbf{x},t) = \tanh\left(\frac{d(\mathbf{x},t)}{\sqrt{2}\epsilon}\right). \tag{11}$$

In the above equation, $d(\mathbf{x}, t)$ is the signed distance function from the interface to $\mathbf{x}$. Note that $\phi(\mathbf{x}, t)$ varies from -0.95 to 0.95, when $d(\mathbf{x}, t)$ is in $(-2\sqrt{2}\epsilon, 2\sqrt{2}\epsilon)$, and $\phi(\mathbf{x}, t) = d(\mathbf{x}, t) = 0$ is the interface of the two phases. Moreover, Eq. (11) is motivated by the equilibrium profile obtained in the thermodynamically derived phase-field model [48–50]. From Eq. (11), we also can compute

$$F(\phi) = \frac{(\phi^2 - 1)^2}{4} = \frac{\epsilon^2}{2}|\nabla\phi|^2, \tag{12}$$

which implies $|\nabla\phi| = (1 - \phi^2)/(\sqrt{2}\epsilon)$. Thus, minimizing $\mathcal{E}_F(\phi)$ forces the phase-field profile to be a hyperbolic tangent profile.

In the modified CH equation given in Eq. (7), the first and second terms are negative gradient descents with respect to the $\dot{H}^{-1}$ and L_2 inner products for the energies $\mathcal{E}_{\mathrm{CH}}(\phi)$ and $\mathcal{E}_F(\phi)$, respectively. Note that Eq. (7) is neither a gradient flow in the $\dot{H}^{-1}$ inner product nor L_2 inner product. For a discussion of CH and gradient flows in $\dot{H}^{-1}$, we refer to Taylor and Cahn [51]. For a discussion of $\mathcal{E}_{\mathrm{CH}}$ in the $\dot{H}^{-1}$ inner product and $\mathcal{E}_F$ in the L_2 inner product, see Bertozzi et al. [9] and the references therein.

Now, we review the derivation of the proposed equation in a 'gradient flow':

$$\phi_t = M\Delta\frac{\delta\mathcal{E}_{\mathrm{CH}}}{\delta\phi} - M\frac{\delta\mathcal{E}_F}{\delta\phi}, \tag{13}$$

where $\mu = \delta\mathcal{E}_{\mathrm{CH}}/\delta\phi$ is the chemical potential that is obtained via the variational derivative of the free energy functional ($\mathcal{E}_{\mathrm{CH}}$) with respect to ϕ, such that

$$\begin{aligned}\frac{d}{d\xi}\mathcal{E}_{\mathrm{CH}}(\phi + \xi\psi)\Big|_{\xi=0} &= \int_\Omega (\psi F'(\phi) + \epsilon^2\nabla\psi\cdot\nabla\phi)d\mathbf{x}\\ &= \int_\Omega (F'(\phi) - \epsilon^2\Delta\phi)\psi\, d\mathbf{x} + \int_{\partial\Omega}\epsilon^2\frac{\partial\phi}{\partial n}\psi\, ds = \int_\Omega (F'(\phi) - \epsilon^2\Delta\phi)\psi\, d\mathbf{x},\end{aligned}$$

where ψ satisfies $\int_\Omega \psi\, d\mathbf{x} = 0$ and $\partial\phi/\partial n$ is zero on $\partial\Omega$. Now, we obtain the chemical potential

$$\mu = \frac{\delta\mathcal{E}_{\mathrm{CH}}}{\delta\phi} = F'(\phi) - \epsilon^2\Delta\phi. \tag{14}$$

By applying the variational derivative of the energy functional $\mathcal{E}_F(\phi)$ with respect to ϕ,

$$\frac{d}{d\xi}\mathcal{E}_F(\phi + \xi\psi)\Big|_{\xi=0} = \lambda\int_\Omega \psi\left(\frac{\phi(\sqrt{2}\epsilon|\nabla\phi| - (1-\phi^2))}{\epsilon^2} + \nabla\cdot\left(-\nabla\phi + \frac{(1-\phi^2)}{\sqrt{2}\epsilon}\frac{\nabla\phi}{|\nabla\phi|}\right)\right)d\mathbf{x},$$

where the Neumann boundary for ϕ, i.e., $\mathbf{n}\cdot\nabla\phi = 0$, is used. Thus,

$$\frac{\delta\mathcal{E}_F}{\delta\phi} = \lambda\frac{\phi(\sqrt{2}\epsilon|\nabla\phi| - (1-\phi^2))}{\epsilon^2} + \lambda\nabla\cdot\left(-\nabla\phi + \frac{(1-\phi^2)}{\sqrt{2}\epsilon}\frac{\nabla\phi}{|\nabla\phi|}\right). \tag{15}$$

Substituting Eqs. (14) and (15) into Eq. (13) yields

$$\frac{\partial\phi}{\partial t} = M\Delta\mu - \frac{\lambda M\phi(\sqrt{2}\epsilon|\nabla\phi| - (1-\phi^2))}{\epsilon^2} + \lambda M\nabla\cdot\left(\nabla\phi - \frac{(1-\phi^2)}{\sqrt{2}\epsilon}\frac{\nabla\phi}{|\nabla\phi|}\right). \tag{16}$$

The total mass conservation $\frac{d}{dt}\int_\Omega \phi d\mathbf{x} = 0$ is important when we solving the incompressible two-phase flows. Verifying mass conservation in Eq. (16) yields

$$\frac{d}{dt}\int_\Omega \phi d\mathbf{x} = \int_\Omega \phi_t d\mathbf{x} = \int_\Omega \frac{-\lambda M\phi(\sqrt{2}\epsilon|\nabla\phi| - (1-\phi^2))}{\epsilon^2}d\mathbf{x} \neq 0.$$

Thus, Eq. (16) does not precisely conserve the mass. However, as mentioned the above, when the phase-field across the interface is a hyperbolic tangent profile, $|\nabla\phi|$ is equal to $(1-\phi^2)/(\sqrt{2}\epsilon)$. The rate of convergence for the total mass conservation in Eq. (16) is reduced. Furthermore, by inspection of Eq. (15), both terms force the interface to be a hyperbolic tangent profile. The first term is to compare the difference between the left side and right side of Eq. (12). The other term is related to diffusion. To achieve total mass conservation and only consider the diffusion effect of the interface, we ignore the second term in Eq. (16) and propose the new modified CH equation given in Eq. (7).

Note that by using Eq. (16), the total free energy $\mathcal{E}(\phi)$ does not strictly decrease in time because $\mathcal{E}_{\mathrm{CH}}(\phi)$ and $\mathcal{E}_F(\phi)$ are minimized in different spaces. Furthermore, Eq. (7) does not force the total energy to be nonincreasing. In fact, to preserve mass conservation and minimize $\mathcal{E}_{\mathrm{CH}}(\phi)$, a fourth-order derivative function in the $\dot{H}^{-1}$-gradient flow of the total free energy $\mathcal{E}(\phi)$ is obtained. However, special care should be taken when discretizing the more complex fourth-order derivative term.

Together with the continuity, phase-field equations, and Navier–Stokes equations, the non-dimensional governing equations are

$$\rho(\phi)(\mathbf{u}_t + \mathbf{u}\cdot\nabla\mathbf{u}) = -\nabla p + \frac{1}{Re}\nabla\cdot(\eta(\phi)(\nabla\mathbf{u} + \nabla\mathbf{u}^T)) + \frac{1}{We}\mathbf{SF} + \frac{\rho(\phi)}{Fr}\mathbf{g}, \tag{17}$$

$$\nabla\cdot\mathbf{u} = 0, \tag{18}$$

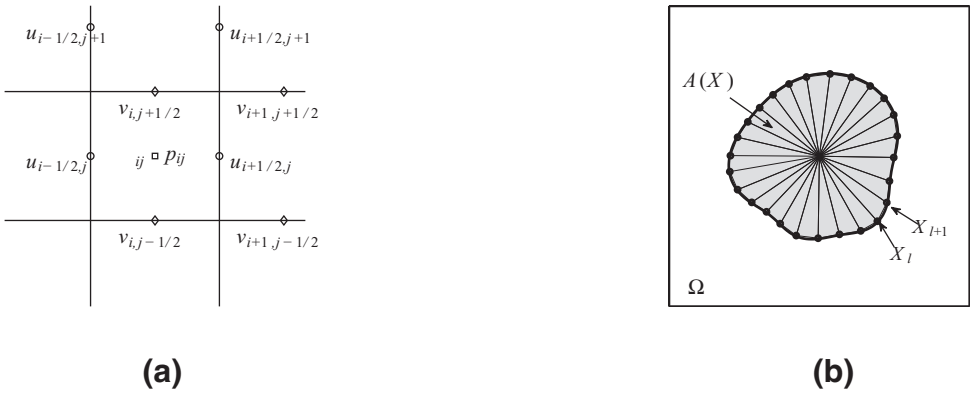

Fig. 3. (a) ϕ and p are defined at the cell center. u and v are defined at the cell edges. (b) Computational polygonal area $A(\phi)$ with boundary points $\mathbf{X}_l = (X_l, Y_l)$ that are located on the zero level of the phase fields, i.e., $A(\phi) = \sum_{l=1}^{N} (X_l Y_{l+1} - Y_l X_{l+1})/2$.

$$\phi_t + \nabla \cdot (\phi \mathbf{u}) = \frac{1}{Pe}\Delta\mu + \frac{\lambda}{Pe}\left(\Delta\phi - \frac{1}{\sqrt{2}\epsilon}\nabla \cdot \left((1-\phi^2)\frac{\nabla\phi}{|\nabla\phi|}\right)\right), \tag{19}$$

$$\mu = \phi^3 - \phi - \epsilon^2\Delta\phi. \tag{20}$$

The dimensionless parameters are the Reynolds number, $Re = \rho_c U_c L_c/\eta_c$, the Weber number, $We = \rho_c L_c U_c^2/\sigma$, the Frounde number, $Fr = U_c/\sqrt{L_c g}$, and the Peclet number, $Pe = U_c L_c/(M\mu_c)$, where L_c is the characteristic length that is taken to be the shortest length of the problem domain in the axial direction, U_c is the characteristic velocity, ρ_c and η_c are the characteristic density and viscosity, respectively, defined as those of fluid 1, i.e., $\rho_c = \rho_1$ and $\eta_c = \eta_1$, and $\mathbf{g} = (0, -1)$ is the gravitational acceleration.

3. Numerical method

An efficient approximation is obtained by decoupling the solution of the momentum equations from the solution of the continuity equation using a projection method [52–54]. We focus on describing this idea in two-dimensional space. The extension to axisymmetric and three-dimensional domains is straightforward. The staggered marker-and-cell (MAC) mesh of Harlow and Welch [55] is used; in this mesh, the pressure and phase fields are stored at the cell centers, and the velocities are stored at cell interfaces (see Fig. 3(a)).

Let ϕ_{ij}^n be an approximation to $\phi(x_i, y_j, n\Delta t)$, where $x_i = (i - 0.5)h$, $y_j = (j - 0.5)h$, h is the space step, and Δt is the time step. The cell vertices are located at $(x_{i+\frac{1}{2}}, y_{j+\frac{1}{2}}) = (ih, jh)$. The discrete differentiation operators are

$$D_x\phi_{i+\frac{1}{2},j} = (\phi_{i+1,j} - \phi_{ij})/h, \quad D_y\phi_{i,j+\frac{1}{2}} = (\phi_{i,j+1} - \phi_{ij})/h,$$

where $\nabla_d\phi_{ij} = (D_x\phi_{i+\frac{1}{2},j}, D_y\phi_{i,j+\frac{1}{2}})$ represents the discrete gradient of ϕ at the cell edges. The discrete divergence operator is defined at cell-center points using values from the cell edges

$$\nabla_d \cdot (u, v)_{ij} = (u_{i+\frac{1}{2},j} - u_{i-\frac{1}{2},j})/h + (v_{i,j+\frac{1}{2}} - v_{i,j-\frac{1}{2}})/h.$$

The discrete five point Laplacian operator (Δ_d) and nine point Laplacian operator (Δ_d^e) can now be defined as

$$\Delta_d\phi_{ij}^{n+1} = (\phi_{i+1,j} + \phi_{i-1,j} + \phi_{i,j+1} + \phi_{i,j-1} - 4\phi_{ij})/h^2,$$
$$\Delta_d^e\phi_{ij}^{n+1} = (\phi_{i+1,j+1}^{n+1} + \phi_{i+1,j-1}^{n+1} + \phi_{i-1,j+1}^{n+1} + \phi_{i-1,j-1}^{n+1} + 4\phi_{i,j-1}^{n+1} + 4\phi_{i,j+1}^{n+1} + 4\phi_{i+1,j}^{n+1} + 4\phi_{i-1,j}^{n+1} - 20\phi_{ij}^{n+1})/(6h^2).$$

We define the total mass, $m(\phi)$ and the polygonal area, $A(\phi)$ by

$$m(\phi) = \sum_{i=1}^{N_x}\sum_{j=1}^{N_y}\phi_{ij}h^2 \quad \text{and} \quad A(\phi) = \sum_{l=1}^{M}(X_l Y_{l+1} - Y_l X_{l+1})/2,$$

where $(X_{M+1}, Y_{M+1}) = (X_1, Y_1)$. Here (X_l, Y_l) for $l = 1, \ldots, M$ are the points that are located on the zero level of the phase fields (see Fig. 3(b)). We obtain these points using the 'contour' commend in MATLAB. At the beginning of each time step, given $\mathbf{u}^n$, ϕ^n, and p^n, we want to find $\mathbf{u}^{n+1}$, ϕ^{n+1}, and p^{n+1} that solve the following temporal discretization of dimensionless form of motion

Eqs. (17)–(20):

$$\rho^n \frac{\mathbf{u}^{n+1}-\mathbf{u}^n}{\Delta t} = -\rho^n(\mathbf{u}\cdot\nabla_d\mathbf{u})^n - \nabla_d p^{n+1} + \frac{1}{We}\mathbf{SF}^n + \frac{\rho^n}{Fr}\mathbf{g} + \frac{1}{Re}\nabla_d\cdot(\eta(\phi)(\nabla_d\mathbf{u}+\nabla_d\mathbf{u}^T))^n, \tag{21}$$

$$\nabla_d\cdot\mathbf{u}^{n+1} = 0,$$
$$\frac{\phi_{ij}^{n+1}-\phi_{ij}^n}{\Delta t} = \frac{1}{Pe}\Delta_d^e\mu_{ij}^{n+1} - \nabla_d\cdot(\phi\mathbf{u})^n + \frac{\lambda}{Pe}\left(\Delta_d^e\phi^n - \frac{1}{\sqrt{2}\epsilon}\tilde{\nabla}_d^c\cdot\left((1-\phi^2)\frac{\nabla_d^c\phi}{|\nabla_d^c\phi|}\right)^n\right), \tag{22}$$

$$\mu_{ij}^{n+1} = (\phi_{ij}^n)^3 - 3\phi_{ij}^n + 2\phi_{ij}^{n+1} - \epsilon^2\Delta_d^e\phi_{ij}^{n+1}. \tag{23}$$

The surface tension force **SF** is discretized as

$$\mathbf{SF}(\phi_{ij}) = -\frac{3\sqrt{2}\epsilon}{4}\tilde{\nabla}_d^c\cdot\left(\frac{\mathbf{m}}{|\mathbf{m}|}\right)_{ij}|\tilde{\nabla}_d^c\phi_{ij}|\tilde{\nabla}_d^c\phi_{ij}.$$

Note that $\mathbf{m}=\nabla_d^c\phi$ is a gradient vector at the cell corner, and $\tilde{\nabla}_d^c\phi_{ij}$ is the gradient vector at grid ij from the cell corner. To discretize the surface tension term, we use nine point terms from the vertex-centered normals:

$$\tilde{\nabla}_d^c\cdot\left(\frac{\mathbf{m}}{|\mathbf{m}|}\right)_{ij} = \frac{1}{2h}\left(\frac{m^x_{i+\frac12,j+\frac12}}{|\mathbf{m}_{i+\frac12,j+\frac12}|} + \frac{m^x_{i+\frac12,j-\frac12}}{|\mathbf{m}_{i+\frac12,j-\frac12}|} - \frac{m^x_{i-\frac12,j+\frac12}}{|\mathbf{m}_{i-\frac12,j+\frac12}|} - \frac{m^x_{i-\frac12,j-\frac12}}{|\mathbf{m}_{i-\frac12,j-\frac12}|}\right.$$
$$\left. + \frac{m^y_{i+\frac12,j+\frac12}}{|\mathbf{m}_{i+\frac12,j+\frac12}|} + \frac{m^y_{i-\frac12,j+\frac12}}{|\mathbf{m}_{i-\frac12,j+\frac12}|} - \frac{m^y_{i+\frac12,j-\frac12}}{|\mathbf{m}_{i+\frac12,j-\frac12}|} - \frac{m^y_{i-\frac12,j-\frac12}}{|\mathbf{m}_{i-\frac12,j-\frac12}|}\right),$$

where $\mathbf{m}_{i+\frac12,j+\frac12}$ is the normal vector at the top right vertex of cell (i,j), which is given by

$$\mathbf{m}_{i+\frac12,j+\frac12} = (m^x_{i+\frac12,j+\frac12}, m^y_{i+\frac12,j+\frac12}) = \left(\frac{\phi_{i+1,j}+\phi_{i+1,j+1}-\phi_{ij}-\phi_{i,j+1}}{2h}, \frac{\phi_{i,j+1}+\phi_{i+1,j+1}-\phi_{ij}-\phi_{i+1,j}}{2h}\right).$$

The other normal vectors are defined in a similar manner. Then, $\tilde{\nabla}_d^c\phi_{ij}$ can be computed as the average of the vertex gradient vector,

$$\tilde{\nabla}_d^c\phi_{ij} = \left(\mathbf{m}_{i+\frac12,j+\frac12} + \mathbf{m}_{i+\frac12,j-\frac12} + \mathbf{m}_{i-\frac12,j+\frac12} + \mathbf{m}_{i-\frac12,j-\frac12}\right)/4.$$

Furthermore, the unit normal vector is defined by $\mathbf{n}_{ij} = \tilde{\nabla}_d^c\phi_{ij}/|\tilde{\nabla}_d^c\phi_{ij}|$. In a similar way, the last term of Eq. (22) at the cell centers from the vertex-centered normals is calculated by

$$\tilde{\nabla}_d^c\cdot\left((1-\phi^2)\frac{\nabla_d^c\phi}{|\nabla_d^c\phi|}\right)_{ij} = \frac{1}{2h}\left((1-\phi^2_{i+\frac12,j+\frac12})\frac{m^x_{i+\frac12,j+\frac12}}{|\mathbf{m}_{i+\frac12,j+\frac12}|} + (1-\phi^2_{i+\frac12,j-\frac12})\frac{m^x_{i+\frac12,j-\frac12}}{|\mathbf{m}_{i+\frac12,j-\frac12}|}\right.$$
$$-(1-\phi^2_{i-\frac12,j+\frac12})\frac{m^x_{i-\frac12,j+\frac12}}{|\mathbf{m}_{i-\frac12,j+\frac12}|} - (1-\phi^2_{i-\frac12,j-\frac12})\frac{m^x_{i-\frac12,j-\frac12}}{|\mathbf{m}_{i-\frac12,j-\frac12}|}$$
$$+(1-\phi^2_{i+\frac12,j+\frac12})\frac{m^y_{i+\frac12,j+\frac12}}{|\mathbf{m}_{i+\frac12,j+\frac12}|} + (1-\phi^2_{i-\frac12,j+\frac12})\frac{m^y_{i-\frac12,j+\frac12}}{|\mathbf{m}_{i-\frac12,j+\frac12}|}$$
$$\left.-(1-\phi^2_{i+\frac12,j-\frac12})\frac{m^y_{i+\frac12,j-\frac12}}{|\mathbf{m}_{i+\frac12,j-\frac12}|} - (1-\phi^2_{i-\frac12,j-\frac12})\frac{m^y_{i-\frac12,j-\frac12}}{|\mathbf{m}_{i-\frac12,j-\frac12}|}\right),$$

where $\phi_{i+\frac12,j+\frac12} = (\phi_{ij}+\phi_{i+1,j}+\phi_{i,j+1}+\phi_{i+1,j+1})/4$, and the other terms are similarly defined. Note that since the last term in Eq. (22) is a fitting term, the same points should be used for the Laplacian operator and divergence operator to reduce numerical errors. Since we are interested in long time simulations, mass conservation is an important factor. Therefore, we use a conservative discretization of the convective part of the phase-field equation in Eq. (22).

$$((\phi u)_x + (\phi v)_y)_{ij}^n = \frac{u^n_{i+\frac12,j}(\phi^n_{i+1,j}+\phi^n_{ij}) - u^n_{i-\frac12,j}(\phi^n_{ij}+\phi^n_{i-1,j})}{2h} + \frac{v^n_{i,j+\frac12}(\phi^n_{i,j+1}+\phi^n_{ij}) - u^n_{i,j-\frac12}(\phi^n_{ij}+\phi^n_{i,j-1})}{2h}.$$

At the beginning of each time step, given $\mathbf{u}^n$ and ϕ^n, we want to find $\mathbf{u}^{n+1}$, p^{n+1}, and ϕ^{n+1} by solving the following discretized equations in time with a projection method.

The outline of the main procedure in one time step is as follows:

Step 1. Initialize ϕ^0 and $\mathbf{u}^0$, the divergence-free velocity field.

Step 2. Solve an intermediate velocity field $\tilde{\mathbf{u}}$ without the pressure gradient term,

$$\rho^n \frac{\tilde{\mathbf{u}} - \mathbf{u}^n}{\Delta t} = -\rho^n \mathbf{u}^n \cdot \nabla_d \mathbf{u}^n + \frac{1}{Re}\Delta_d \mathbf{u}^n + \frac{1}{We}\mathbf{SF}^n + \frac{\rho^n}{Fr}. \tag{24}$$

Step 3. Solve the Poisson equation for the pressure,

$$\nabla_d \cdot \left(\frac{1}{\rho^n}\nabla_d p^{n+1}\right) = \frac{1}{\Delta t}\nabla_d \cdot \tilde{\mathbf{u}}. \tag{25}$$

The resulting linear system of Eq. (25) is solved using a multigrid method [56]. Note that Eq. (25) can be derived by applying the divergence operator to Eq. (26), which is divergence-free:

$$\rho^n \frac{\mathbf{u}^{n+1} - \tilde{\mathbf{u}}}{\Delta t} = -\nabla_d p^{n+1}. \tag{26}$$

Step 4. Update the divergence-free velocity:

$$\mathbf{u}^{n+1} = \tilde{\mathbf{u}} - \frac{\Delta t}{\rho^n}\nabla_d p^{n+1}. \tag{27}$$

Step 5. Implement the proposed numerical scheme in Eqs. (22) and (23) with a nonlinear multigrid method. For a detailed description of the numerical method used to solve these equations, please refer to [57,58]. Steps 1–5 complete one time step.

To satisfy the mass conservation property, i.e., $\sum_{i=1}^{N_x}\sum_{j=1}^{N_y}\phi_{ij}^{n+1} = \sum_{i=1}^{N_x}\sum_{j=1}^{N_y}\phi_{ij}^{n}$, we require

$$\begin{aligned} 0 &= \sum_{i=1}^{N_x}\sum_{j=1}^{N_y}\frac{\phi_{ij}^{n+1} - \phi_{ij}^{n}}{\Delta t} \\ &= \sum_{i=1}^{N_x}\sum_{j=1}^{N_y}\left(\Delta_d^e \mu_{ij}^{n+1} + \lambda\left(\Delta_d^e \phi^n - \frac{1}{\sqrt{2}\epsilon}\tilde{\nabla}_d^c \cdot \left((1-\phi^2)\frac{\nabla_d^c \phi}{|\nabla_d^c \phi|}\right)^n\right)\right). \end{aligned} \tag{28}$$

For $h^2\sum_{i=1}^{N_x}\sum_{j=1}^{N_y}\Delta_d^e\phi_{ij}^{n+1}$, we have

$$\begin{aligned} h^2\sum_{i=1}^{N_x}\sum_{j=1}^{N_y}\Delta_d^e\phi_{ij}^{n} &= h^2\sum_{i=1}^{N_x}\sum_{j=1}^{N_y}\left(\frac{D_x^e\phi_{i+\frac{1}{2},j}^n - D_x^e\phi_{i-\frac{1}{2},j}^n}{h} + \frac{D_x^e\phi_{i,j+\frac{1}{2}}^n - D_x^e\phi_{i,j-\frac{1}{2}}^n}{h}\right) \\ &= h\sum_{j=1}^{N_y}\left(D_x^e\phi_{N_x+\frac{1}{2},j}^n - D_x^e\phi_{\frac{1}{2},j}^n\right) + h\sum_{i=1}^{N_x}\left(D_x^e\phi_{i,N_y+\frac{1}{2}}^n - D_x^e\phi_{i,\frac{1}{2}}^n\right) = 0. \end{aligned}$$

where Eq. (22) and telescoping cancelation are used. $h^2\sum_{i=1}^{N_x}\sum_{j=1}^{N_y}\Delta_d^e\mu_{ij}^{n+1} = 0$ can be proved in a similar manner.

For $h^2\sum_{i=1}^{N_x}\sum_{j=1}^{N_y}\tilde{\nabla}_d^c\cdot((1-\phi^2)\nabla_d^c\phi/|\nabla_d^c\phi|)^n$, we have

$$\begin{aligned} h^2\sum_{i=1}^{N_x}\sum_{j=1}^{N_y}\tilde{\nabla}_d^c \cdot \left((1-\phi^2)\frac{\nabla_d^c\phi}{|\nabla_d^c\phi|}\right)^n &= \frac{h}{2}\sum_{j=1}^{N_y}\left((1-\phi^2_{N_x+\frac{1}{2},j+\frac{1}{2}})\frac{m^x_{N_x+\frac{1}{2},j+\frac{1}{2}}}{|\mathbf{m}_{Nx+\frac{1}{2},j+\frac{1}{2}}|} + (1-\phi^2_{N_x-\frac{1}{2},j-\frac{1}{2}})\frac{m^x_{N_x-\frac{1}{2},j-\frac{1}{2}}}{|\mathbf{m}_{N_x-\frac{1}{2},j-\frac{1}{2}}|}\right. \\ &\quad \left. -(1-\phi^2_{\frac{1}{2},j+\frac{1}{2}})\frac{m^x_{\frac{1}{2},j+\frac{1}{2}}}{|\mathbf{m}_{\frac{1}{2},j+\frac{1}{2}}|} - (1-\phi^2_{-\frac{1}{2},j-\frac{1}{2}})\frac{m^x_{\frac{1}{2},j-\frac{1}{2}}}{|\mathbf{m}_{\frac{1}{2},j-\frac{1}{2}}|}\right) \\ &\quad + \frac{h}{2}\sum_{i=1}^{N_x}\left((1-\phi^2_{i+\frac{1}{2},N_y+\frac{1}{2}})\frac{m^y_{i+\frac{1}{2},N_y+\frac{1}{2}}}{|\mathbf{m}_{i+\frac{1}{2},N_y+\frac{1}{2}}|} + (1-\phi^2_{i-\frac{1}{2},N_y+\frac{1}{2}})\frac{m^y_{i-\frac{1}{2},N_y+\frac{1}{2}}}{|\mathbf{m}_{i-\frac{1}{2},j+\frac{1}{2}}|}\right. \\ &\quad \left. -(1-\phi^2_{i+\frac{1}{2},\frac{1}{2}})\frac{m^y_{i+\frac{1}{2},\frac{1}{2}}}{|\mathbf{m}_{i+\frac{1}{2},\frac{1}{2}}|} - (1-\phi^2_{i-\frac{1}{2},\frac{1}{2}})\frac{m^y_{i-\frac{1}{2},\frac{1}{2}}}{|\mathbf{m}_{i-\frac{1}{2},\frac{1}{2}}|}\right) = 0. \end{aligned}$$

Because of the Neumann boundary condition for ϕ, $m^x_{N_x+\frac{1}{2},j+\frac{1}{2}}$ is zero, and the other terms can be similarly defined. This yields the mass conservation property, which is summarized in Eq. (28).

4. Numerical results

We performed several numerical simulations to demonstrate the performance of our proposed scheme. In particular, we considered translation of a drop, an equilibrium solution with two drops, a convergence test, drops under shear flow, falling

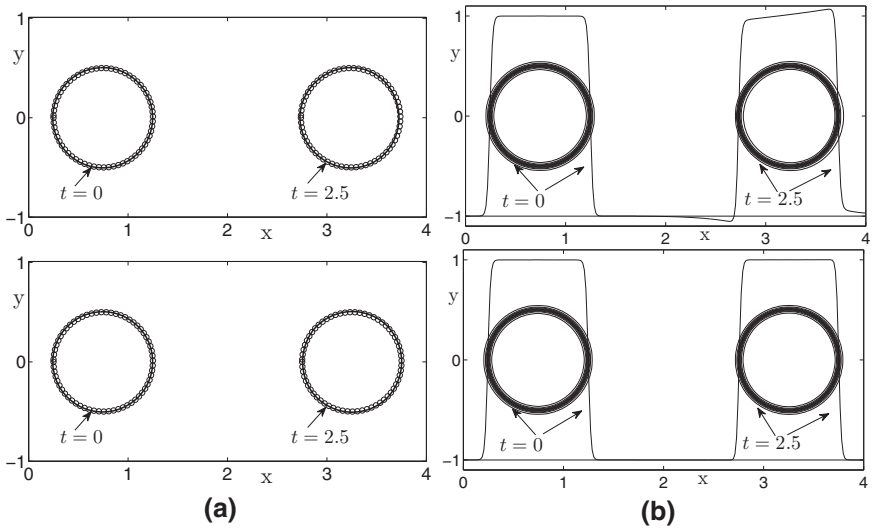

Fig. 4. Translation of a drop with three models. The top and bottom rows are the results from using Eqs. (29) and (30), respectively. (a) Comparison between the zero level of the phase field (line) and exact solution (circle). A constant velocity $\mathbf{u} = (u, v) = (1, 0)$ is used. Note that the exact solution at time t is defined as $(0.2\cos(2\pi l/N) + 0.25 + t, 0.2\sin(2\pi l/N))$, where l is $1, 2, \ldots, N = 400$. (b) Contours are from -0.9 to 0.9 and the lines represent the phase field at plane $y = 0$.

droplets, and the Rayleigh-instability problem. Across the interfacial region, the concentration field varied from -0.9 to 0.9 over a distance of approximately $2\sqrt{2}\epsilon\tanh^{-1}(0.9)$. We used $\epsilon = \epsilon_m = hm/[2\sqrt{2}\tanh^{-1}(0.9)]$, i.e., there were approximately m grid points in the interfacial transition layer.

4.1. Translation of a drop

We consider a translation of a drop with the following two models:

$$\phi_t + \nabla\cdot(\phi\mathbf{u}) = \frac{1}{Pe}\Delta\mu, \tag{29}$$

$$\phi_t + \nabla\cdot(\phi\mathbf{u}) = \frac{1}{Pe}\Delta\mu + \frac{\lambda}{Pe}\left(\Delta\phi - \frac{1}{\sqrt{2}\epsilon}\nabla\cdot\left((1-\phi^2)\frac{\nabla\phi}{|\nabla\phi|}\right)\right). \tag{30}$$

The initial shape is defined as $\phi(x, y, 0) = \tanh\left(\frac{0.5-\sqrt{(x-0.75)^2+y^2}}{\sqrt{2}\epsilon}\right)$, on the domain $(0, 4)\times(-1, 1)$. A constant velocity $\mathbf{u} = (u, v) = (1, 0)$ is given. Furthermore, the parameters $h = 1/128$, $\epsilon_5 \approx 0.00938$, $Pe = 1/\epsilon_5$, and $\lambda = 0.1/\epsilon_5$ are used. We run the simulations up to time $t = 2.5$ with a time step $\Delta t = 5h^2$. A comparison of the two models is shown in Fig. 4. The top and bottom rows are the results from using Eqs. (29) and (30), respectively. In Fig. 4(a), we compare the models to the exact solution. Note that the exact solution at time t is defined as $(X_l, Y_l) = (0.5\cos(2\pi l/N) + 0.75 + t, 0.5\sin(2\pi l/N))$, where l is $1, 2, \ldots, N$ and $N = 400$. Both the CH model and our proposed method yield good results. However, as shown in Fig. 4(b), by using the CH model, the values of ϕ are slightly larger than 1 or smaller than -1 due to the large time step or high velocity. On the other hand, our proposed model completely eliminates numerical errors.

4.2. Effect of parameter λ

In this section, we study the effect of parameter λ in Eq. (30) on the dynamics of a translating droplet with $\lambda = 1/\epsilon_5, 0.1/\epsilon_5, 0.01/\epsilon_5$ and $\Delta t = 0.5h^2$. The other parameters and initial condition are the same as those in Section 4.1. To compare the exact solution with the numerical solutions obtained by using different values of λ at time $t = 2.5$, we put them together in Fig. 5. In the case of $\lambda = 1/\epsilon_5$, the drop does not preserve a circular shape. The reason is likely that the larger λ leads to reduce the effect of the CH equation, because $|\nabla\phi|$ is approximately, but not exactly, equal to $(1-\phi^2)/(\sqrt{2}\epsilon)$ in Eqs. (7) and (12). The CH equation reduces these differences as evidenced by the definition of $\mathcal{E}_{\mathrm{CH}}(\phi)$. Furthermore, theoretically, ϕ should be in $[-1, 1]$; however, this may be violated when the advection term is added. If ϕ is much larger than 1 or smaller than -1, the second term in Eqs. (7) and (10) does not force ϕ to be 1 or -1, since both $1-\phi^2$ and $-|\nabla\phi|$ are negative. Thus, the CH equation should be used to force ϕ to be 1 or -1. In the case of $\lambda = 0.01/\epsilon_5$, the accuracy is slightly lower than that obtained by using $\lambda = 0.1/\epsilon_5$.

Furthermore, we investigate the effect of λ on the results with different Pe and ϵ. All parameters is the same as above except the value of parameters for λ, Pe and ϵ. Table 1 shows the l_2-norm errors with $\lambda = 1/\epsilon, 0.1/\epsilon, 0.01/\epsilon$ and $Pe = 10/\epsilon, 1/\epsilon, 0.1/\epsilon$. Here $\epsilon = \epsilon_5$ is fixed. The discrete l_2-norm of error is defined as $\sqrt{\frac{1}{N}\sum_{l=1}^{N}\left(\sqrt{(X_l-3.25)^2+Y_l^2}-0.5\right)^2}$, where X_l and Y_l are nu-

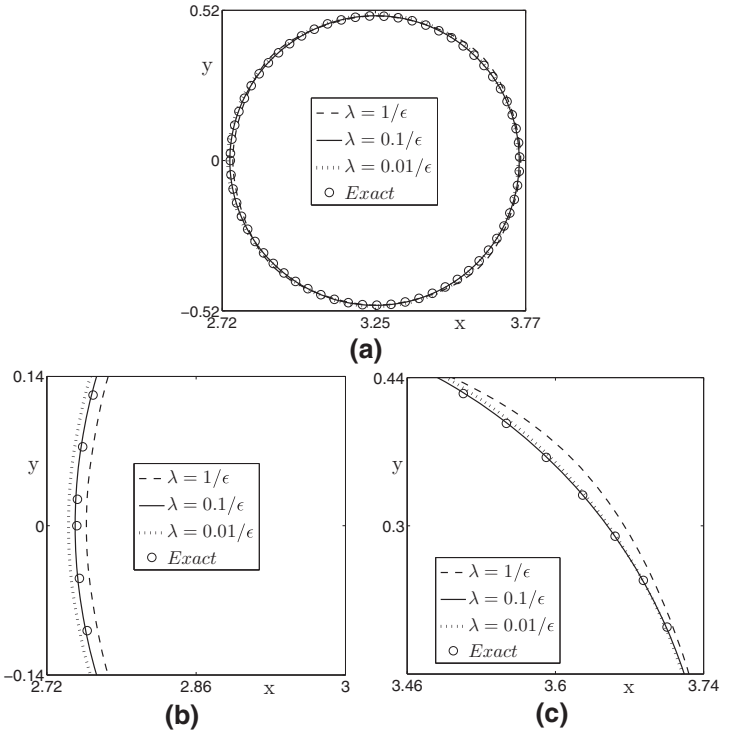

Fig. 5. Mesh plots of ϕ obtained using $\lambda = 0.01/\epsilon_5, 0.1/\epsilon_5$, and$1/\epsilon_5$ at time $t = 2.5$. (a) Whole view. (b) and (c) Closeup views.

Table 1
l_2-norm errors with various λ and *Pe*. Here $\epsilon = \epsilon_5$ is fixed.

Case	$\lambda = 1/\epsilon$	$\lambda = 0.1/\epsilon$	$\lambda = 0.01/\epsilon$
$Pe = 10/\epsilon$	8.395E−3	6.671E−3	1.030E−2
$Pe = 1/\epsilon$	5.288E−3	2.404E−3	5.941E−3
$Pe = 0.1/\epsilon$	7.572E−3	5.753E−3	9.697E−3

merical results. From Table 1 we can see that the larger *Pe* or smaller *Pe* will low the accuracy of numerical solutions. For a fixed *Pe*, $\lambda = 0.1/\epsilon$ is a better choice than $1/\epsilon$ and $0.01/\epsilon$.

Fig. 6 (a) shows the l_2 normal errors at time $t = 2.5$ with different $\epsilon = \epsilon_3, \epsilon_5, \epsilon_8$, and ϵ_{10}. For a chosen ϵ, we perform the numerical experiments with five different values $\lambda = 1/\epsilon, 0.5/\epsilon, 0.1/\epsilon, 0.05/\epsilon$, and $0.01/\epsilon$. The solid lines in Fig. 6(a) are polynomial fittings of data points and the circle symbol denotes the minimal l_2 errors obtained from the polynomial fitting profile. For a chosen ϵ, we also can find the best value of λ, which corresponds to circle symbol. Fig. 6(b) shows the fitting plot of the approximate best value of λ and $1/\epsilon$. To compare with the profile of $\lambda = 0.1/\epsilon$, we put them together. We can see that the values are similar for small ϵ, but deviate significantly for large ϵ. Also note that for much larger ϵ may give unphysical values of surface tension because the thickness ϵ should be small and theoretically approach to zero. For the rest of the paper, we will simply use $\lambda = 0.1/\epsilon$.

4.3. Equilibrium solution with two drops

We consider the equilibrium solution for two drops without fluid. The initial shape is defined as

$$\phi(x, y, 0) = \tanh\left(\frac{0.2 - \sqrt{(x-0.3)^2 + (y-0.5)^2}}{\sqrt{2}\epsilon}\right) + \tanh\left(\frac{0.1 - \sqrt{(x-0.75)^2 + (y-0.5)^2}}{\sqrt{2}\epsilon}\right) + 1,$$

on the domain $(0, 1) \times (0, 1)$. The parameters $h = 1/128$, $\Delta t = 0.1h^2$, ϵ_5, and $Pe = 1$ are used. Fig. 7 shows the zero contour plots of the phase field, which are obtained by the CH model and our proposed model. Clearly, by using the CH model, the small drop shrinks and the large one grows. This is because the CH model was originally proposed to simulate the spinodal decomposition of a binary mixture [59]. Spinodal decomposition is a mechanism by which a solution of two or more components separates into different phases. The CH model works by shifting the interface of two divided drops as shown in Fig. 7(a). In the absence of viscous, gravitational, surface tension force, or other external forces, the divided drops are gathered together, which is perfectly

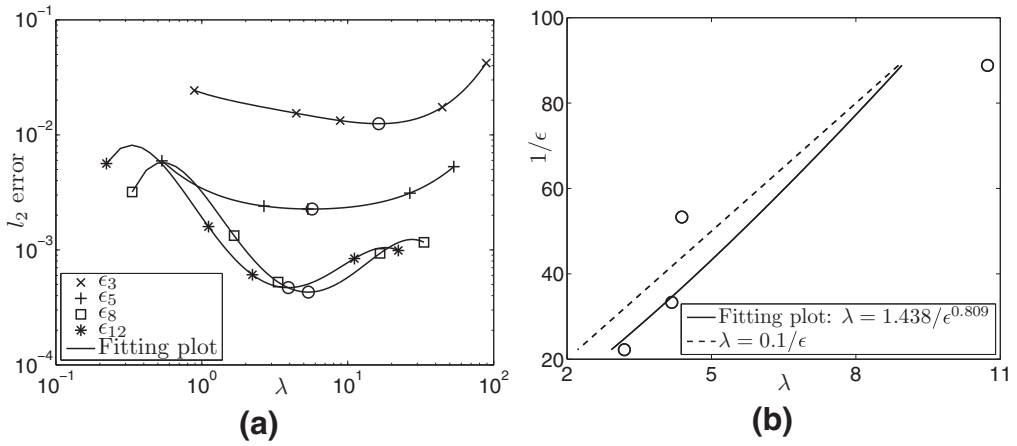

Fig. 6. (a) l_2-norm errors with $\epsilon = \epsilon_3, \epsilon_5, \epsilon_8, \epsilon_{10}$ and $\lambda = 1/\epsilon, 0.5/\epsilon, 0.1/\epsilon, 0.05/\epsilon, 0.01/\epsilon$. Note that the solid lines are polynomial fitting of data points and the circle symbol denotes the minimal l_2 errors obtained from the polynomial fitting profile. (b) The fitting plot of the best value of λ and $1/\epsilon$. Here the best value of λ corresponds to circle symbol in (a).

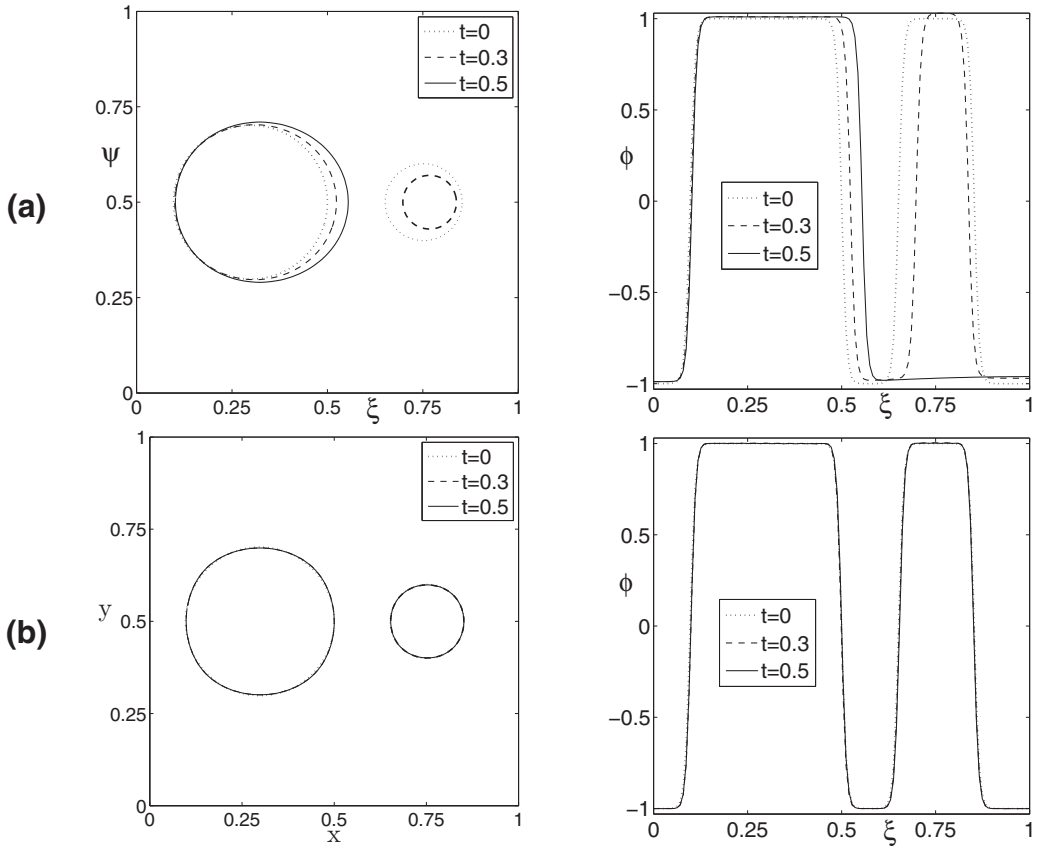

Fig. 7. Mesh plots of the phase-field profiles for the CH equation (a) and proposed equation (b). The whole view is on the left, and the plane view is on the right.

permissible within the CH framework but would be impossible in the physical context. On the other hand, with the interface correction term, the two divided drops remain as shown in Fig. 7(b).

Fig. 8 shows comparison of total energy obtained by the CH model and our proposed method. Note that for better visualization purposes, we multiply $\mathcal{E}_F$ by 100 (see solid line). With the original CH equation, the total energy $\mathcal{E}_{CH}$ is decreasing in time. The total energy is generally reduced by shrinking the bulk ϕ and shifting the location of the interface. While our propose model forces the interfacial profile to remain a hyperbolic tangent profile. Thus in this numerical test, the total energy $\mathcal{E}_{CH}$ obtained by our proposed method is almost constant and the two divided drops remain.

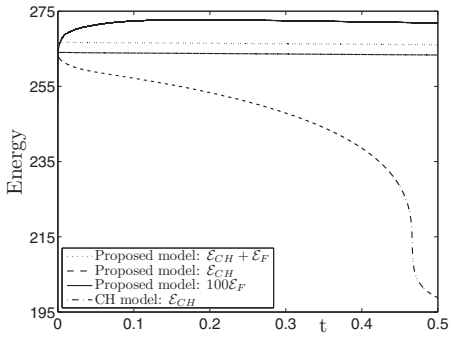

Fig. 8. Comparison of total energy obtained by the CH model and our proposed method. Note that for better visualization purposes, we multiply $\mathcal{E}_F$ by 100 (see solid line).

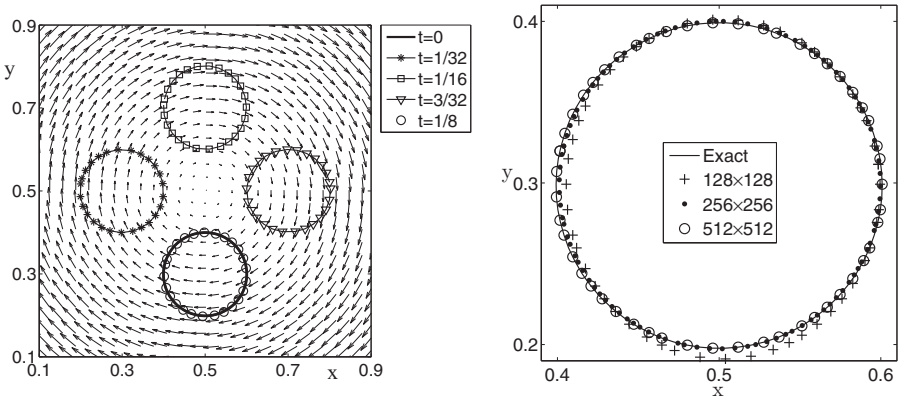

Fig. 9. A rotated disk by background fluids flows. (a) Evolution of the disk, where the velocity field and drop coincide. (b) Convergence of the numerical results with refined spatial and temporal grids.

Table 2
Error and convergence results with various mesh grids and time steps ($\Delta t = h^2$).

Case	128×128		256×256		512×512
Proposed method: l_2-error	2.746E−2		6.334E−3		1.602E−3
Proposed method: rate		2.11		1.98	
Original CH : l_2-error	7.335E−2		2.012E−2		5.125E−3
Original CH : rate		1.87		1.97	

4.4. Convergence test

To obtain an estimate of the convergence rate, we perform a number of simulations on a set of increasingly finer grids $h = 1/2^n$ for $n = 6, 7$, and 8 on the domain $\Omega = (0, 1) \times (0, 1)$. We consider the passive advection of a disk by the background velocity field, such as

$$\mathbf{u} = (u, v) = (16\pi\,(y - 0.5), -16\pi\,(x - 0.5)). \tag{31}$$

The disk with radius 0.1 is centered at (0.5, 0.3). The other parameters are set as ϵ_5 and $\Delta t = h^2$. The circle is returned to its initial position by inverting the velocity field at time $t = 1/8$. Note that the circle should not change its shape as a result of the rotation. Fig.9(a) illustrates the evolution of the drop by the background fluid flow. In Fig. 9(b), we compare the results obtained using different mesh grids at time $t = 1/4$. By observation, the convergence of the results under spatial and temporal refinements is evident.

We define the error of a grid as the discrete l_2-norm of the difference between the numerical solution and the exact solution as follows: $e_{hij} := \phi_{hij} - \overset{0}{\phi}_{hij}$. The rate of convergence is defined as the ratio of successive errors: $\log_2 (\|e_h\|_2 / \|e_{\frac{h}{2}}\|_2)$. Since we refined the spatial and temporal grids by a factor of 4 and 2, respectively, the ratio of successive errors increases by a factor of 2. The errors and rates of convergence obtained using these definitions are given in Table 2. Second-order accuracy with respect to space and first-order accuracy with respect to time is observed, as expected from the discretization. To compare with the original

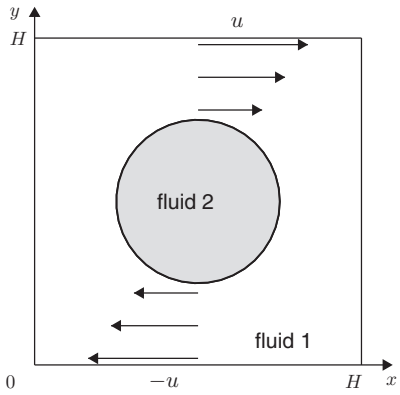

Fig. 10. Schematic illustration of the initial condition.

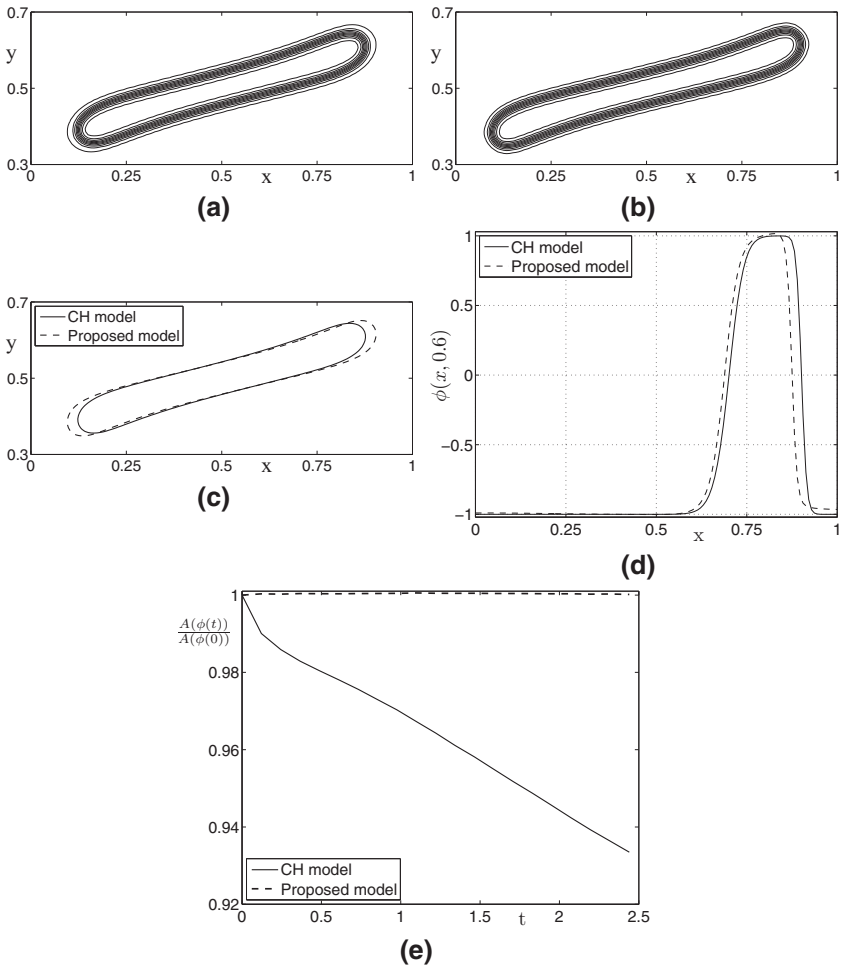

Fig. 11. Drop shape under shear flow obtained by the CH model and the proposed model at time $t = 2.44$. (a) CH model, (b) Proposed model. The contours are from −0.9 to 0.9 for (a) and (b). (c) Overlay of both results at the zero level. (d) Plots of $\phi(x, 0.6)$ obtained by two mentioned methods. (e) Normalized polygonal area with the CH model and proposed model.

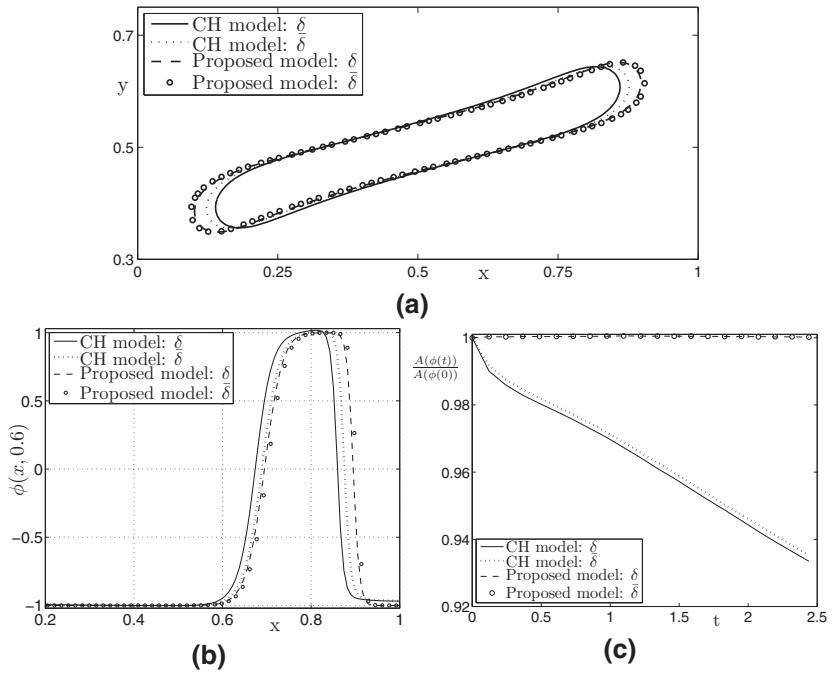

Fig. 12. Comparison between delta functions δ and $\bar{\delta}$. (a) Zero contour of ϕ at time 2.44. (b) Plots of $\phi(x, 0.6)$. (c) Temporal evolution of the normalized polygonal areas.

CH model, we put them together in Table 2. These results suggest that the numerical scheme for the original CH model is indeed second order accurate in space. While its l_2-error compared with our proposed method is higher.

4.5. Drops under shear flow

Next, we investigate the deformation of drops under shear flow. The top moves to the right with velocity u and the bottom moves to the left with velocity $-u$ in the computational domain $\Omega = (0, H) \times (0, H)$. Fig. 10 shows a schematic illustration of the initial condition.

We begin with a drop of radius 0.15 positioned at the center of the computational domain $\Omega = (0, 1) \times (0, 1)$. In this simulation we take the following parameters: $Re = 50$, $We = 100$, $Pe = 1/\epsilon_5$, and $u = 1$. The ratios of the density and viscosity are both equal to 1. A mesh size of 128×128 and a time step of $\Delta t = 5h^2$ are used. Fig. 11 shows the drop shape under shear flow obtained by the CH model and proposed model at time $t = 2.44$. In Fig. 11 (a) and (b), the contours of the phase field are from -0.9 to 0.9. Observing the results in Fig. 11(b), the interface profile at the droplet ends are not uniform because of the high velocity. Thus, the surface tension increases as the interface thins but decreases as the interface thickens. To force the interface to be uniform, the CH diffusion effect, i.e., the motion by minus the Laplacian of the mean curvature is added in a non-physical context. Thus, the droplet ends obtained by the original CH model are shorter compared to our proposed method as shown in Fig. 11 (c). Due to the large time step or high velocity at the tip of drop, by using the CH model ϕ inside and outside of drop are significantly smaller than -1 and 1, respectively, as shown in Fig. 11 (d). However with our proposed method, ϕ remains in $[-1, 1]$. In Fig. 11 (e), we show the area change with two methods. As can be seen that though two methods hold mass conservation property on the whole domain, the area $A(\phi)$ obtained by the CH model is not conserved. On the other hand, approximate mass conservation for the zero level is achieved using our proposed method.

Since the used delta function $\delta = \epsilon\alpha|\nabla\phi|^2$ scales with interface thickness, it may be not accurate if the interface profile deviates from the desired tanh-profile. Here, we will consider a delta function $\bar{\delta} = 0.5|\nabla\phi|$, which scales independent of interface thickness. All parameters and initial condition are the same as the above test except $\bar{\delta}$. Fig. 12 shows the comparison between delta functions δ and $\bar{\delta}$. From these results, we can see that the result obtained by delta function $\bar{\delta}$, which is independent of interface thickness, is more accurate than that from δ.

4.6. Falling droplet

In this section, we consider two falling droplets. A smaller drop with radius $r = 0.05$ is positioned at (0.5, 2.9) and a large bubble with radius $r = 0.15$ is set at (0.5, 2.3) in the computational domain $\Omega = (0, 1) \times (0, 3)$. The densities are $\rho_1 = 1$ and $\rho_2 = 3$. The other parameters are defined as following: ϵ_5, $Re = 50$, $Pe = 1/\epsilon_5$, $Fr = 1$, $h = 1/128$, and $\Delta t = 5h^2$. To simulate the falling droplets, we use periodic boundary condition to the vertical boundaries and a no slip boundary condition to the top

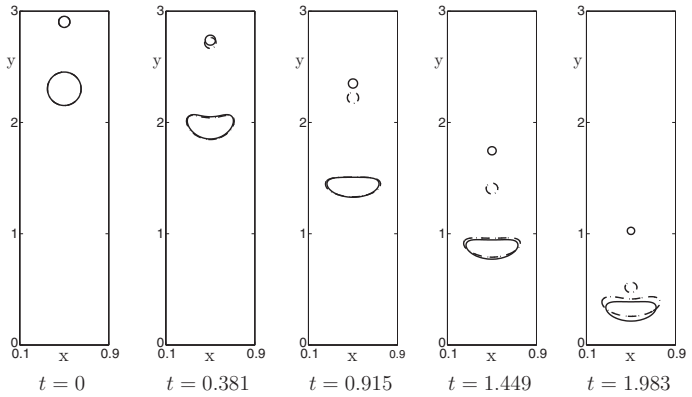

Fig. 13. Falling droplets. The solid and dashed lines are the results obtained by the CH model and our proposed model, respectively. The computational times are shown below each figure.

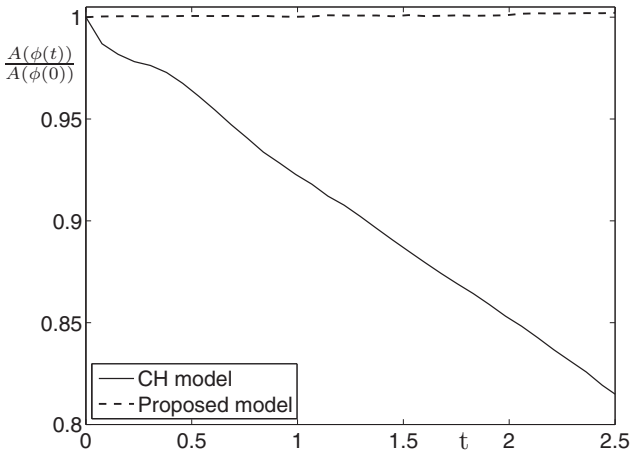

Fig. 14. Temporal evolution of the normalized polygonal areas from two methods for the falling droplets.

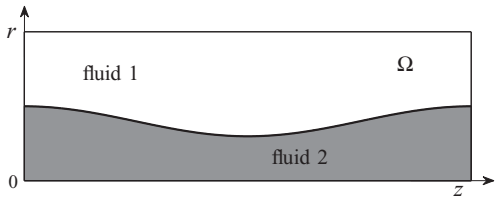

Fig. 15. A schematic illustration of the Rayleigh-instability problem.

and bottom boundaries. Fig. 13 shows that the drops fall due to buoyancy. To compare our proposed model with the CH model, we put the results from the two models together. The solid and dashed lines are the results obtained by the CH model and the proposed model, respectively. We can observe that the proposed model is better in preserving the area of the smaller droplet. Fig. 14 shows the comparison of the polygonal areas from two methods. We can see that by using the CH model, the polygonal area losses for the large and small drops are as large as 10.0% and 57.2%, respectively. On the other hand, our proposed method significantly reduces the polygonal area loss.

4.7. Rayleigh-instability problem

Surface tension causes a fluid to have as little surface area as possible for a given volume. A long slender column of liquid reduces its surface area by breaking up into a series of small droplets, which have less surface area than the cylinder [31]. This effect is known as Rayleigh-instability [60]. In this section, we consider a long cylindrical shape and simulate it in the axisymmetric domain. A schematic illustration of the Rayleigh-instability problem is shown in Fig. 15.

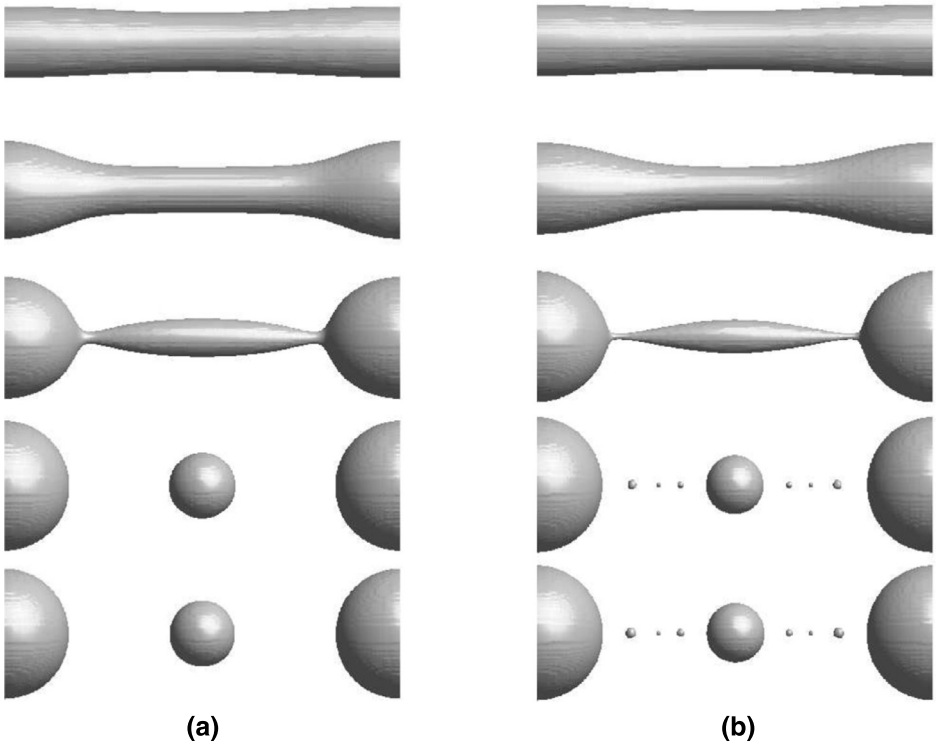

Fig. 16. Evolution of the Rayleigh-instability problem. (a) CH model. (b) Our proposed model. From top to bottom, the dimensional times are $t = 0, 0.45, 0.75, 1.2,$ and, 2.85.

The initial phase field and velocity fields are given by

$$\phi(r, z, 0) = \tanh\left(\frac{r - 0.5 - 0.05\cos(z)}{\sqrt{2}\epsilon}\right),$$
$$\mathbf{u}(r, z, 0) = 0.$$

on the domain, $\Omega = \{(r, z) | 0 \le r \le \pi \text{ and } 0 \le z \le 2\pi\}$ with 128×256 mesh grids. For this computation, we choose the parameters: $\epsilon_5, Re = 0.5, We = 0.01, Pe = 1/\epsilon_5, \Delta t = 0.05h^2$, viscosity ratio 0.25 and density ratio 1. The interface profiles obtained by the CH model and our proposed model are shown in Fig. 16. The zone of the minimum moves symmetrically off the center ($z = \pi$), giving rise to satellite drops. These satellite drop formations can be attributed to the nonlinear terms in the equations of motion [61]. From Fig. 16(b), notice that by using our proposed method, the smaller drops rise from the effect of surface tension and remain with long-time evolution. On the other hand, the divided smaller drops disappear when the CH equation is used. It is well-known that the CH equation describes the process of phase separation, by which two components of a binary fluid spontaneously separate and form in each component [1,59]. Thus, it is difficult to maintain divided smaller drops with the original CH equation.

5. Conclusions

In this paper, we presented a new phase-field fluid model and computation with minimized CH dynamics. The new modified CH model was proposed with an interface correction term to force the interface profile to be a hyperbolic tangent function. As we mentioned in Section 1, there are three drawbacks of the standard method. An interface with a hyperbolic tangent profile is important because of the surface tension formulation. Under the advection of flow, the interface of two phases may be not a hyperbolic tangent profile. To enforce the interface to be uniform, the CH diffusion effect, i.e., the motion by minus the Laplacian of the mean curvature will be added in the non-physical context. Even though the original CH dynamics conserves the total mass, the conservation of the enclosed area obtained by its interface can not remain. Several numerical examples such as translation of a drop, an equilibrium solution with two drops, a convergence test, drops under shear flow, falling droplets, and the Rayleigh-instability problem were presented to demonstrate that our present method reduce these three drawbacks. As a future research work, it would be interesting to investigate the effect of surface tension formula on the fluid dynamics.

Acknowledgment

Y.B. Li is supported by the Fundamental Research Funds for the Central Universities, China. J.-I. Choi was supported by the National Research Foundation of Korea (NRF) grant funded by the Korea government (MSIP) (No. NRF20151009350). The corresponding author (J.S. Kim) was supported by the National Research Foundation of Korea (NRF) grant funded by the Korea government (MSIP) (NRF-2014R1A2A2A01003683). The authors are grateful to the reviewers whose valuable suggestions and comments significantly improved the quality of this paper.

References

[1] Cahn JW, Hilliard JE. Free energy of a nonuniform system. i: interfacial free energy. J Chem Phys 1958;2:258–67.
[2] Fife PC. Models for phase separation and their mathematics. Electron J Differ Equ 2000;48:1–26.
[3] Kim J. A continuous surface tension force formulation for diffuse-interface models. J Comput Phys 2005;204:784–804.
[4] Brassel M, Bretin E. A modified phase field approximation for mean curvature flow with conservation of the volume. Math Methods Appl Sci 2011;34:1157–80.
[5] Marconi UMB, Tarazona P. Dynamic density functional theory of fluids. J Chem Phys 1999;110:8032–44.
[6] Folch R, Casademunt J, Hernández-Machado A. Branching transition in viscous fingering with a liquid crystal. In: Branching in Nature. Centre de Physique des Houches, vol. 14; 2001. p. 439–44.
[7] Wise SM, Lowengrub JS, Frieboes H, Cristini V. Three-dimensional multispecies nonlinear tumor growth: I. Model and numerical method. J Theor Biol 2008;253:524–43.
[8] Cristini V, Li X, Lowengrub JS, Wise SM. Nonlinear simulations of solid tumor growth using a mixture model: invasion and branching. J Math Biol 2009;58:723–63.
[9] Bertozzi A, Esedoglu S, Gillette A. Inpainting of binary images using the Cahn–Hilliard equation. IEEE Trans Image Process 2007;16:285–91.
[10] Bertozzi AL, Esedoglu S, Gillette A. Analysis of a two-scale Cahn–Hilliard model for image inpainting. Multiscale Model Simul 2007;3:913–36.
[11] Li Y, Shin J, Choi Y, Kim J. Three-dimensional volume reconstruction from slice data using phase-field models. Comput Vision Image Und 2015. doi:10.1016/j.cviu.2015.02.001.
[12] Aland S. Time integration for diffuse interface models for two-phase flow. J Comput Phys 2014;262:58–71.
[13] Badalassi VE, Ceniceros HD, Banerjee S. Computation of multiphase systems with phase field models. J Comput Phys 2003;190:371–97.
[14] Boyer F, Lapuerta C, Minjeaud S, Piar B, Quintard M. Cahn–Hilliard/Navier–Stokes model for the simulation of three-phase flows. Transp Porous Media 2010;82:463–83.
[15] Biben T, Misbah C. Tumbling of vesicles under shear flow within an advected-field approach. Phys Rev E 2003;67:031908.
[16] Bao K, Shi Y, Sun S, Wang XP. A finite element method for the numerical solution of the coupled Cahn–Hilliard and Navier–Stokes system for moving contact line problems. J Comput Phys 2012;231:8083–99.
[17] Di Y, Li R, Tang T. A general moving mesh framework in 3d and its application for simulating the mixture of multi-phase flows. Commun Comput Phys 2008;3:582–603.
[18] Ding H, Spelt DDM, Shu C. Diffuse interface model for incompressible two-phase flows with large density ratios. J Comput Phys 2007;226:2078–95.
[19] Ding H, Spelt DDM. Onset of motion of a three-dimensional droplet on a wall in shear flow at moderate Reynolds numbers. J Fluid Mech 2008;599:341–62.
[20] Ding H, Spelt DDM. Wetting condition in diffuse interface simulations of contact line motion. Phys Rev E 2007;75:046708.
[21] Teigen KE, Song P, Lowengrub J, Voigt A. A diffuse-interface method for two-phase flows with soluble surfactants. J Comput Phys 2011;230:375–93.
[22] Folch R, Casademunt J, Hernandez-Machado A, Ramirez-Piscina L. Phase-field model for Hele-Shaw flows with arbitrary viscosity contrast. I. Theoretical approach. Phys Rev E 1999;60:1724.
[23] Folch R, Casademunt J, Hernandez-Machado A, Ramirez-Piscina L. Phase-field model for Hele-Shaw flows with arbitrary viscosity contrast. II. Numerical study. Phys Rev E 1999;60:1734.
[24] Allen SM, Cahn JW. A microscopic theory for antiphase boundary motion and its application to antiphase domain coarsening. Acta Metall 1979;27:1085–95.
[25] Gao M, Wang XP. A gradient stable scheme for a phase field model for the moving contact line problem. J Comput Phys 2012;231:1372–86.
[26] Li Y, Jeong D, Shin J, Kim J. A conservative numerical method for the Cahn–Hilliard equation with Dirichlet boundary conditions in complex domains. Comput Math Appl 2013;65:102–15.
[27] Lee C, Jeong D, Shin J, Li Y, Kim J. A fourth-order spatial accurate and practically stable compact scheme for the Cahn–Hilliard equation. Physica A 2014;409:17–28.
[28] Khatavkar VV, Anderson PD, Duineveld PC, Meijer HE. Diffuse-interface modelling of droplet impact. J Fluid Mech 2007;581:97–127.
[29] Kim J. Phase field computations for ternary fluid flows. Comput Methods Appl Mech Eng 2007;196:4779–88.
[30] Kim J. A generalized continuous surface tension force formulation for phase-field models for multi-component immiscible fluid flows. Comput Methods Appl Mech Eng 2009;198:3105–12.
[31] Kim J, Kang K, Lowengrub J. Conservative multigrid methods for Cahn–Hilliard fluids. J Comput Phys 2004;193:511–43.
[32] Kim J. Phase-field models for multi-component fluid flows. Commun Comput Phys 2014;12:613–61.
[33] Liu J, Dedé L, Evans JA, Borden MJ, Hughes TJR. Isogeometric analysis of the advective Cahn–Hilliard equation: spinodal decomposition under shear flow. J Comput Phys 2013;242:321–50.
[34] Lee HG, Kim KM, Kim J. On the long time simulation of the Rayleigh–Taylor instability. Int J Numer Methods Eng 2011;85:1633–47.
[35] Liu C, Shen J. A phase–field model for the mixture of two incompressible fluids and its approximation by a Fourier-spectral method. Physica D 2003;179:211–28.
[36] Menech MD. Modeling of droplet breakup in a microfluidic *t*-shaped junction with a phase-field model. Phys Rev E 2006;73:031505.
[37] Shen J, Yang XF. A phase-field model and its numerical approximation for two-phase incompressible flows with different densities and viscosities. SIAM J Sci Comput 2010;32:1159–79.
[38] Whitesides GM. The origins and the future of microfluidics. Nature 2006;442:368–73.
[39] Xu Z, Huang H, Li X, Meakin P. Phase field and level set methods for modeling solute precipitation and/or dissolution. Comput Phys Commun 2012;183:15–19.
[40] Yue PT, Feng JJ, Liu C, Shen J. A diffuse-interface method for simulating two-phase fows of complex fuids. J Fluid Mech 2004;515:293–317.
[41] Yue PT, Feng JJ, Liu C, Shen J. Interfacial forces and Marangoni flow on a nematic drop retracting in an isotropic fluid. J Colloid Interface Sci 2005;290:281–8.
[42] Yue PT, Feng JJ. Wall energy relaxation in the Cahn-Hilliard model for moving contact lines. Phys Fluids 2011;23:012106.
[43] Zhang Y, Wang H, Tang T. Simulating two-phase viscoelastic flows using moving finite element methods. Commun Comput Phys 2010;7:333–49.
[44] Zhou C, Yue PT, Feng JJ, Ollivier-Gooch CF, Hu HH. 3d phase-field simulations of interfacial dynamics in Newtonian and viscoelastic fluids. J Comput Phys 2010;229:498–511.
[45] Cahn JW, Elliott CM, Novick-Cohen A. The Cahn-Hilliard equation with a concentration dependent mobility: motion by minus the Laplacian of the mean curvature. Eur J Appl Math 1996;7:287–301.
[46] Yue PT, Zhou C, Feng JJ. Spontaneous shrinkage of drops and mass conservation in phase-field simulations. J Comput Phys 2007;223:1–9.
[47] Zhang J, Du Q. Numerical studies of discrete approximations to the Allen–Cahn equation in the sharp interface limit. SIAM J Sci Comput 2009;31:3042–63.
[48] Boettinger WJ, Warren JA, Beckermann C, Karma A. Phase-field simulation of solidification. Ann Rev Mater Res 2002;32:163–94.

[49] Ilmanen T. Convergence of the Allen-Cahn equation to Brakke's motion by mean curvature. J Differ Geom 1993;38:417–61.
[50] Evans LC, Soner HM, Souganidis P. Phase transitions and generalized motion by mean curvature. Commun Pure Appl Math 1992;45:1097–123.
[51] Taylor JE, Cahn JW. Linking anisotropic sharp and diffuse surface motion laws via gradient flows. J Stat Phys 1994;77:183–97.
[52] Bell JB, Colella P, Glaz HM. A second-order projection method for the incompressible Navier-Stokes equations. J Comput Phys 1989;85:257–83.
[53] Chorin AJ. A numerical method for solving incompressible viscous flow problems. J Comput Phys 1967;2:12–26.
[54] Li J, Renardy Y. Numerical study of flows of two immiscible liquids at low Reynolds number. SIAM Rev 2000;42:417–39.
[55] Harlow FH, Welch JE. Numerical calculation of time–dependent viscous incompressible flow of fluid with free surface. Phys Fluids 1965;8:2182–9.
[56] Trottenberg U, Oosterlee C, Schüller A. Multigrid. USA: Academic Press; 2001.
[57] Kim J. A numerical method for the Cahn–Hilliard equation with a variable mobility. Commun Nonlinear Sci Numer Simul 2007;12:1560–71.
[58] Kim J, Bae HO. An unconditionally gradient stable adaptive mesh refinement for the Cahn–Hilliard equation. J Korean Phys Soc 2008;53:672–9.
[59] Cahn JW. On spinodal decomposition. Acta Mater 1961;9:795–801.
[60] Rayleigh WS. On the stability, or instability, of certain fluid motions. Proc London Math Soc 1878;10:4–13.
[61] Chacha M, Radeev S, Tadrist L, Occelli R. Numerical treatment of the instability and the breakup of a liquid capillary column in a bounded immiscible phase. Int J Multiphase Flow 1997;23:377–95.